

## Research Article

# Preparation and Characterization of Pt-Doped Bi<sub>2</sub>MoO<sub>6</sub> Nanocomposites and Its High PDT Efficiency on HL60 Cells

Mucang Xiao, Miaomiao Li, Yongkun Lun, Qilin Pan, Baoquan Ai, and Jianwen Xiong 

School of Physics and Telecommunication Engineering, South China Normal University, Guangzhou 510006, China

Correspondence should be addressed to Jianwen Xiong; [jwxiong@scnu.edu.cn](mailto:jwxiong@scnu.edu.cn)

Received 17 September 2021; Revised 16 November 2021; Accepted 22 November 2021; Published 11 December 2021

Academic Editor: Haisheng Qian

Copyright © 2021 Mucang Xiao et al. This is an open access article distributed under the Creative Commons Attribution License, which permits unrestricted use, distribution, and reproduction in any medium, provided the original work is properly cited.

In this study, Pt-doped Bi<sub>2</sub>MoO<sub>6</sub> nanocomposites were prepared by solvothermal and in situ reduction method. We used XRD, UV-Vis spectroscopy, TEM, EDS, and XPS to characterize its chemical properties. Results showed that the Pt-doped Bi<sub>2</sub>MoO<sub>6</sub> nanocomposites had advantages of small size, good dispersion, and wide spectral response range. Then, we tested its biological toxicity and PDT efficiency on HL60 cells. Both pure Bi<sub>2</sub>MoO<sub>6</sub> and Pt-doped Bi<sub>2</sub>MoO<sub>6</sub> nanocomposites showed great biocompatibility after coincubated with leukemia cells for 12 h in the dark. As to PDT efficiency, Pt-doped Bi<sub>2</sub>MoO<sub>6</sub> had a better-inactivated effect than pure Bi<sub>2</sub>MoO<sub>6</sub>. Furthermore, the PDT efficiency went up when atomic ratios and concentration increased. While the atomic ratio was 5% and the concentration was 1000 μg/mL, it reached the highest value at 85.2%. At last, we briefly analyzed the photocatalysis mechanism, which demonstrated that it was a potential photosensitizer with high efficiency for treating leukemia.

## 1. Introduction

Cancer is a global problem that imposes a growing health and economic burden on human society [1]. Leukemia is the most common cancer in children [2]. However, the efficacy of conventional chemotherapeutic agents is low, and the disease carries a poor prognosis with frequent relapses and high mortality [3]. In recent years, photodynamic therapy (PDT) and photothermal therapy (PTT) are becoming promising therapeutic methods for cancer treatment as they have advantages of mild trauma, low toxic, and short treatment period [4–10]. The mechanism of photodynamic therapy is that the photosensitizers are delivered to tumor through intravenous injection and then locally stimulated by the specific wavelength of light. At this time, photosensitizers absorbed lots of energy to produce a series of reactive oxygen species (ROS) and then damage tumor cells [11]. Therefore, photosensitizer is an important component in the process of photodynamic therapy. How to improve its PDT efficiency remains to a challenging problem for researchers.

As a common photosensitizer, TiO<sub>2</sub> has been widely studied in the last few years [12, 13]. However, it can only be excited by ultraviolet and near-ultraviolet light (which makes up only 5% of sunlight) as its band gap usually above 3.0 eV. In order to exploit the energy of light source more efficiently, a variety of bismuth-based semiconductors have been developed, such as Bi<sub>2</sub>O<sub>3</sub> [14], Bi<sub>2</sub>MoO<sub>6</sub> [15–18], Bi<sub>2</sub>O<sub>2</sub>CO<sub>3</sub> [19, 20], and BiOX (X = Cl, Br, I) [21–23]. As a fascinating Aurivillius phase material, Bi<sub>2</sub>MoO<sub>6</sub> has been the hotspot in photocatalytic applications due to its visible light absorption, nontoxicity, low cost, and high chemical durability [24]. So it has been extensively used in the fields of photocatalytic hydrogen production [25] and degradation of organic pollutants [26]. However, pure Bi<sub>2</sub>MoO<sub>6</sub> suffers from low efficiency in separating photogenerated carriers, small surface area, and poor quantum yield, resulting in low photocatalytic activity. Various strategies, such as morphology control [27–29], doping/defect-introduction [30], metal deposition [31, 32], and semiconductor combination [33], have been systematically explored to improve the photocatalytic activity. Among these methods, metal

deposition is one of the most effective and simple ways to improve its performance.

In this study, pure  $\text{Bi}_2\text{MoO}_6$  and Pt-doped  $\text{Bi}_2\text{MoO}_6$  nanocomposites were first used as photosensitizer to inactivate the leukemia cells. In our research,  $\text{Bi}_2\text{MoO}_6$  nanoparticles were prepared by solvothermal method using  $\text{Bi}(\text{NO}_3)_3 \cdot 5\text{H}_2\text{O}$  and  $(\text{NH}_4)_6\text{Mo}_7\text{O}_{24} \cdot 4\text{H}_2\text{O}$  as precursors, and then Pt-doped  $\text{Bi}_2\text{MoO}_6$  nanocomposites were prepared by in situ reduction method. The chemical properties were characterized by XRD, UV-Vis spectroscopy, TEM, EDS, and XPS. Then, we tested their biological toxicity in dark and PDT efficiency and analyzed its mechanism of inactivation. The experimental results showed that the Pt-doped  $\text{Bi}_2\text{MoO}_6$  nanocomposites had low dark toxicity and high inactivation efficiency on human HL60 leukemia cells.

## 2. Materials and Methods

**2.1. Materials and Apparatus.** Ammonium hydroxide ( $\text{NH}_3 \cdot \text{H}_2\text{O}$ ) and glycerol were purchased from Tianjin ZhiYuan Reagent Co., Ltd. (Tianjin, China). Bismuth nitrate ( $\text{Bi}(\text{NO}_3)_3 \cdot 5\text{H}_2\text{O}$ ) was purchased from Xilong Scientific Co., Ltd. (Shantou, China). Ammonium molybdate ( $(\text{NH}_4)_6\text{Mo}_7\text{O}_{24} \cdot 4\text{H}_2\text{O}$ ) and chloroplatinic acid hexahydrate ( $\text{H}_2\text{PtCl}_6 \cdot 6\text{H}_2\text{O}$ ) were purchased from Macklin Biochemical Technology Co., Ltd. (Shanghai, China). HL60 cells were obtained from the Academy of Military Medical Sciences. RPMI-1640 medium was purchased from KeyGEN BioTECH (Jiangsu, China). Cell Counting Kit-8 (CCK-8) assay was purchased from Dojindo (Shanghai, China). Reactive Oxygen Species Assay Kit was bought from Applygen (Beijing, China). All chemicals were used without further purification. Deionized water used in the synthesis was from local sources.

Apparatuses used for characterization of Pt-doped  $\text{Bi}_2\text{MoO}_6$  nanocomposites are BRUKER D8 ADVANCE X-ray powder diffractometer (XRD) (Bruker, Germany), U-3010 UV-visible spectrophotometer (Hitachi, Japan), JEM-2100HR transmission electron microscope (JEOL, Japan), ZEISS Gemini-500 scanning electron microscope (Carl Zeiss, Germany), laser particle size analyzer (provided by South China Normal University), AXIS Ultra X-ray photoelectron spectroscopy (XPS) (Kratos, UK), and Wfy-28 fluorescent spectrophotometer (Tuopu, China). Apparatuses used for photodynamic therapy in vitro are PDT reaction chamber (designed by our laboratory), Model 680 microplate reader (Bio-Rad, USA), HH.CP-TW80 CO<sub>2</sub> incubator (Bluepard, China), DK-8D electric-heated thermostatic bath (Yiheng, China), and KA-1000 centrifuge (Anke, China).

**2.2. Preparation of Pure  $\text{Bi}_2\text{MoO}_6$  (Pure BMO) and Pt-Doped  $\text{Bi}_2\text{MoO}_6$  (Pt-BMO) Samples.** The pure BMO was synthesized by solvothermal method. In a typical procedure, 5.0 mmol (2.425 g)  $\text{Bi}(\text{NO}_3)_3 \cdot 5\text{H}_2\text{O}$  and 0.36 mmol (0.445 g)  $(\text{NH}_4)_6\text{Mo}_7\text{O}_{24} \cdot 4\text{H}_2\text{O}$  were dissolved in 60 ml glycerol (at 50°C) [34]. Stir the solvent until the crystallizations were absolutely dissolved in glycerol. Then, dribble 5%  $\text{NH}_3$  (aq.) slowly to make the pH value adjusted to 9. After the mixture turn a nontransparent milky white, transfer it into

a 100 ml Teflon-lined stainless steel autoclave, and heat the mixture at 140°C for 24 h in an oven. Then centrifugate the yellow-brown product at 10000 rpm, and wash it with deionized water and absolute ethanol four times. After that, the sediment was dried at 80°C in oven. Finally, the powder was calcined at 400°C for 2 h to remove the organic residues. At this time, pure BMO was obtained, and it looked very granular and golden.

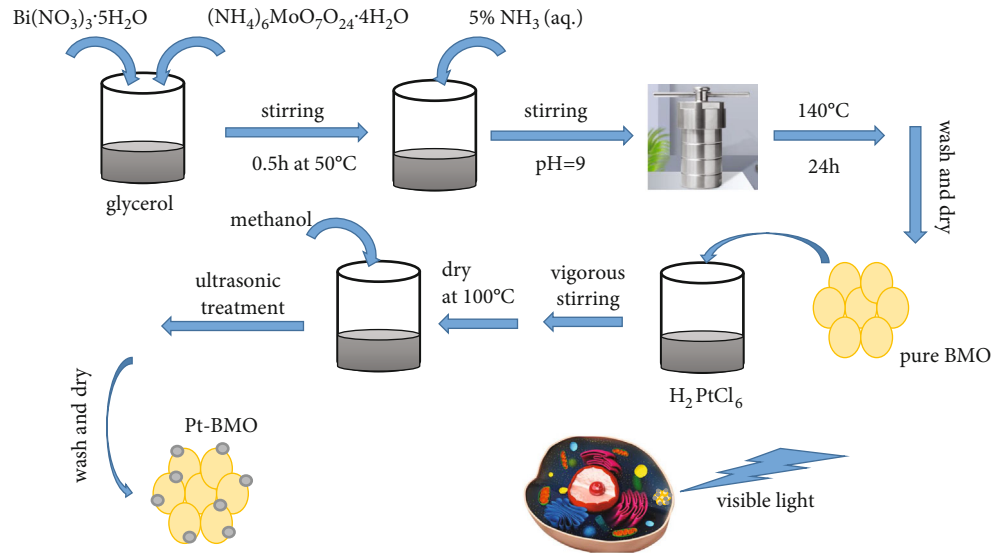
The Pt-BMO samples were synthesized by in situ reduction method, as shown in Scheme 1. The as-prepared pure BMO (0.5 mmol) was well dispersed in 30 ml  $\text{H}_2\text{PtCl}_6$  solutions under vigorous magnetic stirring for 1 h. Then, the mixture was dried at 100°C for 12 h. When the temperature cooled down at 25°C spontaneously, the dried mixture was immersed in 30 ml methanol under ultrasonic concussion for 0.5 h. The precipitate was washed though deionized water several times and dried at 80°C for 8 h. The as-prepared samples were named as 1%Pt-BMO, 2%Pt-BMO, and 5%Pt-BMO. All the percentages are the atomic ratio.

**2.3. Photocatalytic Activity Measurements.** Photocatalytic degradation of RhB was conducted in a beaker at room temperature. Photocatalyst (100 mg) was added into the beaker containing 100 mL RhB aqueous solution with the initial concentration of 10 mg/L. Prior to irradiation, the solution was magnetically stirred in dark for 1 h to establish an adsorption-desorption equilibrium between photocatalyst and RhB. Then, the suspension was irradiated by a 300 W Xenon lamp with a 420 nm cut-off filter from the top of beaker. During the photoreaction, the reaction photocatalysts were collected at 30 min intervals and then centrifuged to remove the solid photocatalysts. The ratios ( $C/C_0$ ) of the RhB evaluate the degradation rate by detecting the absorbance spectra at 553 nm by a UV-vis spectrophotometer.

**2.4. Cell Resuscitation.** Human leukemia HL60 cells were frozen in ultralow temperature storage (-81°C) before experiment. The frozen cells were thawed in electric-heated thermostatic bath (37°C) for several minutes. Then, the turbid solution was centrifuged at 1000 rpm for 10 min, so the HL60 cells were collected on the bottom of centrifugal tube. Then, cells were transferred into petri dish which contained RPMI 1640 medium and were subsequently placed in humidified incubator with 5% CO<sub>2</sub> at 37°C. When cells propagated at the logarithmic stage, it can be used for the following experiment.

**2.5. Evaluation of Cell Activity.** The CCK-8 method has advantages of short testing time, convenient operation, high sensitivity, and excellent reproducibility [35]. So it was chosen for the evaluation of HL60 cells viability. The CCK-8 (20  $\mu\text{L}$ ) was added in cell suspension (200  $\mu\text{L}$ ); then, the mixture was replaced in the CO<sub>2</sub> incubator for one to four hours. The absorbance (OD value) will be obtained by Model 680 Microplate Reader at 450 nm.

**2.6. Biological Toxicity for Pure BMO and Pt-BMO Samples to HL60 Cells.** The 96 hole plate was used to contain cell solution and nanoparticle solution (the prepared nanocomposites were dispersed in RPMI-1640 medium). For more



SCHEME 1: Schematic diagram for preparing Pt-BMO nanocomposites for photodynamic therapy.

elaborative, every type of nanocomposites was dissolved in culture medium with different concentrations (200  $\mu\text{g/mL}$ , 400  $\mu\text{g/mL}$ , 600  $\mu\text{g/mL}$ , 800  $\mu\text{g/mL}$ , and 1000  $\mu\text{g/mL}$ ). The test included blank group, control group, and experimental group. The blank group consisted of culture medium (20  $\mu\text{L}$ ); the control group was composed of culture medium (10  $\mu\text{L}$ ) and cell solution (10  $\mu\text{L}$ ); the experimental group consisted of cell solution (10  $\mu\text{L}$ ) and nanoparticles solution (10  $\mu\text{L}$ ). Each group had three duplications to get the mean value. After, solutions were seeded in the 96 hole plate, and it was placed on oscillator for 1 minute and then transferred into the  $\text{CO}_2$  incubator for 12 h. Finally, the CCK-8 method was used to measure the biological toxicity of pure BMO and Pt-BMO samples. The relative viability of cells was figured out by the following equation:

$$R = \frac{\text{OD}_{\text{treated}} - \text{OD}_{\text{blank}}}{\text{OD}_{\text{control}} - \text{OD}_{\text{blank}}} \cdot 100\%, \quad (1)$$

where  $\text{OD}_{\text{treated}}$ ,  $\text{OD}_{\text{control}}$ , and  $\text{OD}_{\text{blank}}$  refer to the OD value of experimental group, control group, and blank group, respectively.  $R$  means the relative viability of cells.

**2.7. Experiment Design for Photodynamic Therapy.** It is necessary to prepare two 96 hole plates. Two plates were seeded with cell solution (10  $\mu\text{L}$ ) and nanoparticles solution (10  $\mu\text{L}$ ). Nanoparticle solutions (pure BMO, 1%Pt-BMO, 2%Pt-BMO, and 5%Pt-BMO) with different concentrations (200  $\mu\text{g/mL}$ , 400  $\mu\text{g/mL}$ , 600  $\mu\text{g/mL}$ , 800  $\mu\text{g/mL}$ , and 1000  $\mu\text{g/mL}$ ) were set to find out which is best for photodynamic therapy. Each group had three duplications to get the mean value. After solutions were well mingled, two plates were placed in the  $\text{CO}_2$  incubator 12 h to ensure that nanoparticles can intrude into cytoplasm. Then, one plate was transferred in PDT reaction chamber to get irradiated for 1 h, and another plate was cultivated in  $\text{CO}_2$  incubator as before.

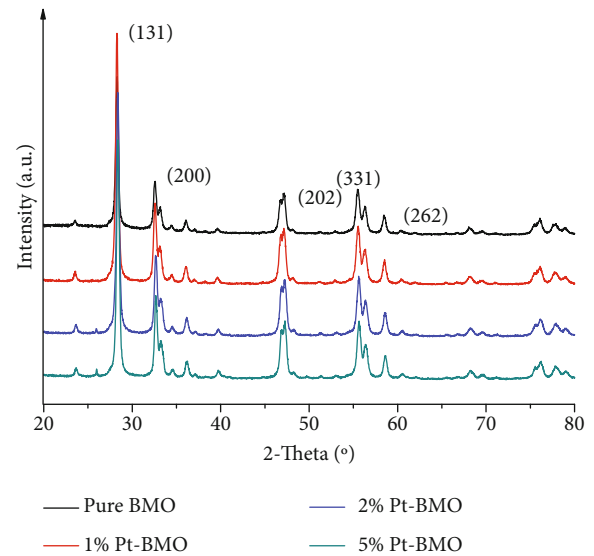


FIGURE 1: XRD patterns of pure BMO and Pt-BMO samples with different atomic ratio.

Finally, the CCK-8 method was used to measure the PDT efficiency, and it can be figured out by the following equation:

$$P_e = 1 - \frac{\text{OD}_{\text{irradiated}}}{\text{OD}_{\text{nonirradiated}}} \cdot 100\%, \quad (2)$$

where  $\text{OD}_{\text{irradiated}}$  and  $\text{OD}_{\text{nonirradiated}}$  refer to the OD value of irradiated group and nonirradiated group.  $P_e$  is the PDT efficiency.

**2.8. Statistical Analysis.** Data are represented as means  $\pm$  SD (standard deviation) from three independent experiments. The statistical software SPSS 25 is chosen for performing statistical analysis. When the value of  $P$  is less than 0.05, data are perceived statistically significant.

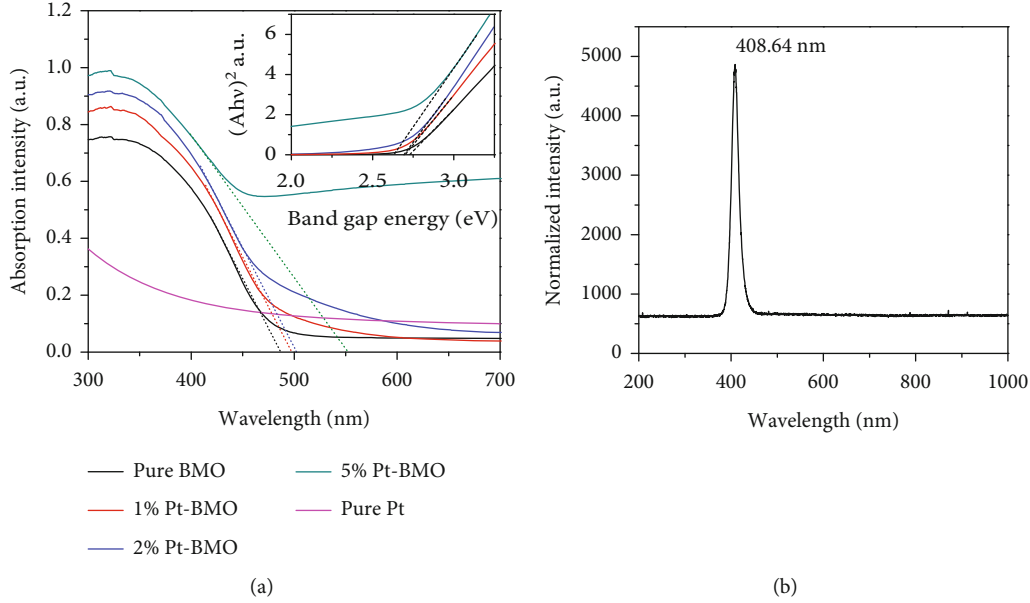


FIGURE 2: (a) UV-Vis spectra of pure BMO, pure Pt, and Pt-BMO nanocomposites; the inset shows the band gap energy of the pure BMO and Pt-BMO samples. (b) The emission spectrum of the light source.

### 3. Results and Discussion

#### 3.1. Characterization of Pt-BMO Nanocomposites

**3.1.1. X-Ray Diffraction.** The crystal structure of a sample is an important factor for its structural characteristics. Therefore, we characterized the samples by XRD to analyze its crystalline phase. As Figure 1 shows, the XRD diffraction peaks of the pure BMO and Pt-BMO nanocomposites appeared at  $2\theta$  of  $28.3^\circ$ ,  $23.6^\circ$ ,  $33.1^\circ$ ,  $46.8^\circ$ ,  $47.1^\circ$ ,  $55.6^\circ$ ,  $56.4^\circ$ , and  $58.5^\circ$ , which can be indexed to the characteristic peaks (131), (002), (060), (202), (062), (133), (191), and (262) of orthorhombic phase  $\text{Bi}_2\text{MoO}_6$ . For samples of Pt-BMO nanocomposites, its diffraction peak did not shift when compared with the pure BMO, indicating that Pt did not enter the lattice of  $\text{Bi}_2\text{MoO}_6$ , in other words, it existed on the surface of  $\text{Bi}_2\text{MoO}_6$ . The diffraction peaks of the four samples were all sharp and high, and there were no extra peaks, manifesting that the samples possess high crystallinity and high purity. No diffraction peak of metal Pt was found in the XRD pattern of Pt-BMO, perhaps this was due to the simple fact that the content of metal Pt was too slight to be detected. In addition, the characteristic peak became stronger with the content of Pt increase, which further testified to the successful preparation of Pt-BMO nanocomposites.

According to the Scherrer formula [36]:

$$D = \frac{k\lambda}{\beta \cos \theta}, \quad (3)$$

where  $D$  is the crystalline size,  $\lambda$  is the X-ray wavelength,  $k$  is the constant (it is generally regarded as 0.89),  $\beta$  is the width of the diffraction line at half of the maximum intensity. As for the sample of pure BMO,  $2\theta = 28.27^\circ$ ,  $\beta = 0.366^\circ$ ,

so the particle size was 22.1 nm at average. These calculated results were certainly in agreement with TEM test results. The particle size of 2%Pt-BMO nanocomposites was 21.6 nm, which was slightly smaller than the pure BMO.

**3.1.2. UV-Vis Spectroscopy.** The UV-visible absorption spectra of the pure BMO and Pt-BMO samples were measured by UV-2550 UV-visible spectrophotometer. The results were represented in Figure 2(a). Evidently, pure Pt shows low absorption ability in visible light region. The absorption peak of four nanocomposite samples is located around 340 nm, and the value of it got higher as the content of Pt increased. As for pure BMO, its spectral response range was mainly distributed lower than 475 nm. However, after Pt doping, it can be red-shifted to the visible region in different degrees. The onset of absorption spectrum for 1%Pt-BMO, 2%Pt-BMO, and 5%Pt-BMO nanocomposites was 482 nm, 501 nm, and 570 nm, respectively. The values of band gap energy ( $E_g$ ) were calculated by the equation  $Ah\nu = \alpha(h\nu - E_g)^{n/2}$  [37], where  $A$  is the absorption coefficient near the absorption edge;  $h$  is the Planck constant with the unit of eV;  $\alpha$  is a constant;  $E_g$  is the absorption band gap energy.  $\text{Bi}_2\text{MoO}_6$  is a direct band gap semiconductor, thus  $n = 1$  [38]. The inset of Figure 2(a) shows curves of  $(Ahv)^2$  plots versus photon energy ( $h\nu$ ) of pure BMO, 1%Pt-BMO, 2%Pt-BMO, and 5%Pt-BMO nanocomposites. The band gap of 1%Pt-BMO, 2%Pt-BMO, and 5%Pt-BMO was estimated to be about 2.69 eV, 2.68 eV, and 2.57 eV, respectively, which implied that the adsorption edges of Pt-BMO samples shifted towards visible region in comparison to that of pure BMO (2.72 eV). So, the Pt-BMO samples can be excited by light with longer wavelength. In order to reach a high photocatalytic inactivation efficiency, an in-house built lamp with many high-power light-emitting diodes (LEDs), emitting

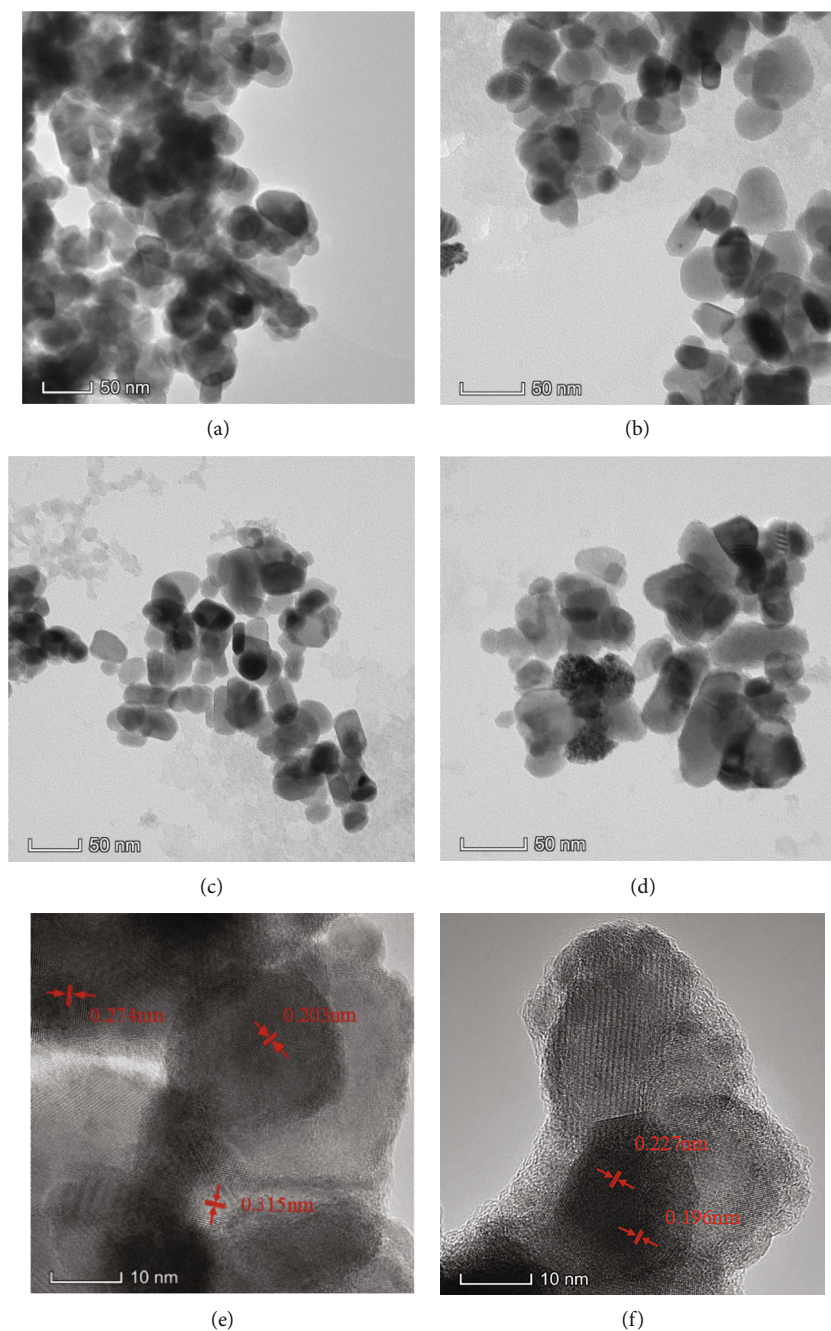


FIGURE 3: TEM images of (a) pure BMO, (b) 1%Pt-BMO, (c) 2%Pt-BMO, (d) 5%Pt-BMO and the amplified image of (e) pure BMO and (f) 5%Pt-BMO nanocomposites.

light in the visible light region 392–420 nm and with a peak at 408.64 nm, was taken as light sources for PDT in the experiments, as Figure 2(b) shows. The light density at the position of the sample was  $5 \text{ mW/cm}^2$ , and the light irradiation time lasts for 1 h.

**3.1.3. TEM Studies.** The particle size and lattice spacing were analyzed by JEM-2100HR transmission electron microscope. Figures 3(a)–3(d) display the TEM images of pure BMO and Pt-BMO. As Figure 3(a) represented, the size of pure BMO was ranged from 20 to 50 nm with low dispersion.

With the increase of Pt metal concentration, the dispersity of nanocomposites has been improved. After doping with Pt, the morphology of the nanocomposites did not change significantly. Figure 3(e) is an amplified image of pure BMO. The interplanar spacings of 0.315 nm, 0.274 nm, and 0.203 nm correspond to the (131), (002), and (080) lattice planes of orthorhombic phase  $\text{Bi}_2\text{MoO}_6$ . In Figure 3(f), the interplanar spacings of 0.196 nm and 0.227 nm correspond to the (200) and (111) lattice planes of metal Pt, indicating that Pt has been successfully loaded on the pure BMO sample.

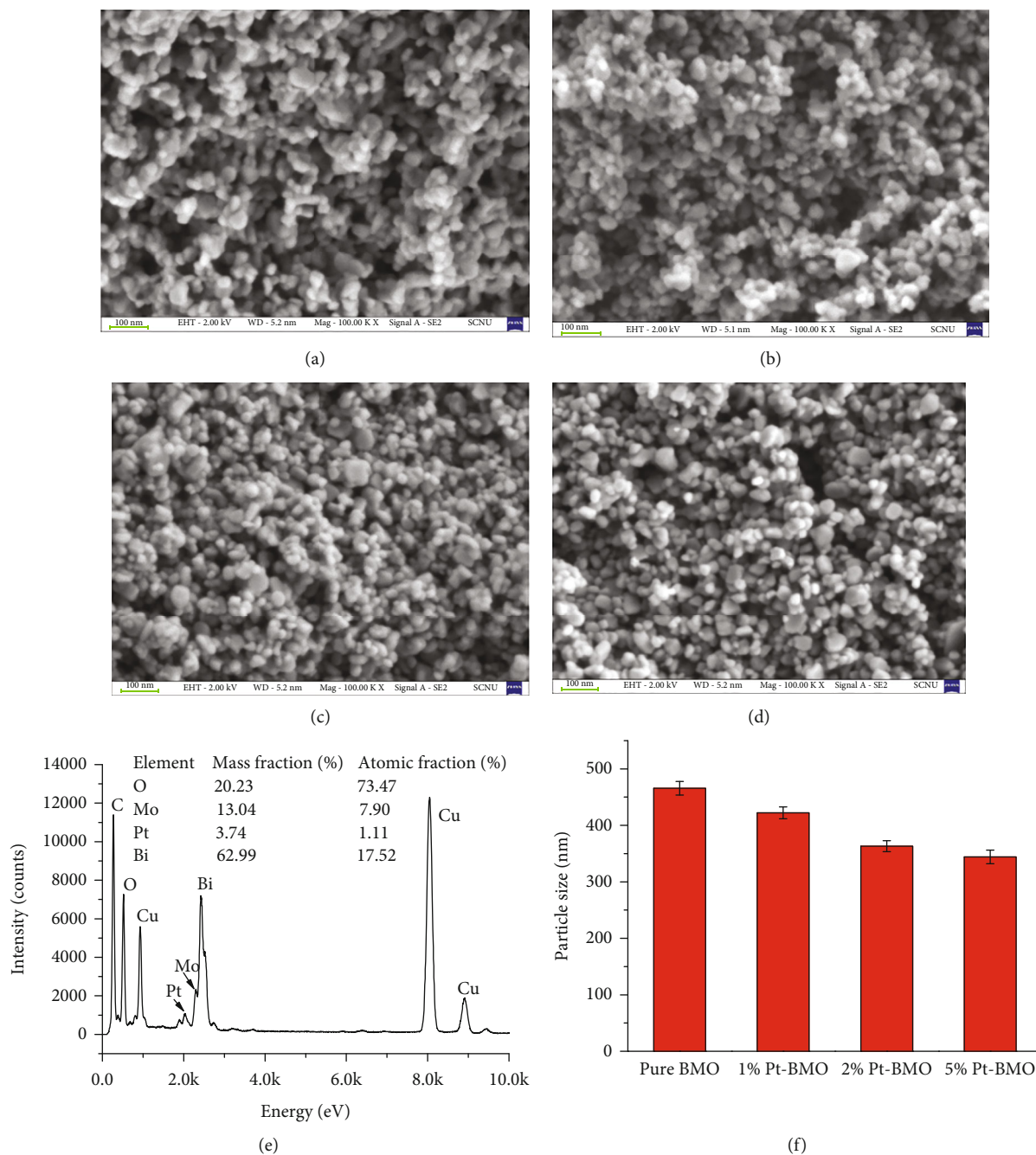


FIGURE 4: SEM images of (a) pure BMO, (b) 1%Pt-BMO, (c) 2%Pt-BMO, (d) 5%Pt-BMO; the energy dispersive spectrogram of (e) 1%Pt-BMO; the hydrodynamic size of (f) Pt-BMO nanocomposites in average.

**3.1.4. SEM Observation and Particle Size Analysis.** The morphology of pure BMO and Pt-BMO nanocomposites was observed with scanning electron microscope, and the laser particle size analyzer was used to test the hydrodynamic size. The SEM images were displayed in Figures 4(a)–4(d). It appears that the loading of Pt can efficiently inhibit agglomeration of  $\text{Bi}_2\text{MoO}_6$ . The morphology of  $\text{Bi}_2\text{MoO}_6$  did not change after Pt doping, which proved that Pt was simply deposited on the surface. The energy dispersive spectrum (EDS) of 1% Pt-BMO nanocomposites was tested in order to analyze the element content. As Figures 4(e) shows, the peaks of Pt, Bi, Mo, and O indicated

that the samples were mainly composed of Bi, Mo, O, and a small amount of Pt. The mass ratios of O, Mo, Pt, and Bi were 20.23%, 13.04%, 3.74%, and 62.99%, and the atomic ratios were 73.47%, 7.90%, 1.11%, and 17.52%, respectively. The appearance of Cu may be caused by the use of copper mesh during sample testing. Figure 3(f) showed the hydrodynamic size distribution of pure BMO and Pt-BMO samples. On account of agglomeration, nanocomposites had larger particle size than it was represented in TEM. The average size for pure BMO is 465.8 nm, and that for 5%Pt-BMO is 344.1 nm. Obviously, the doping of Pt can improve dispersity of nanocomposites in solution.

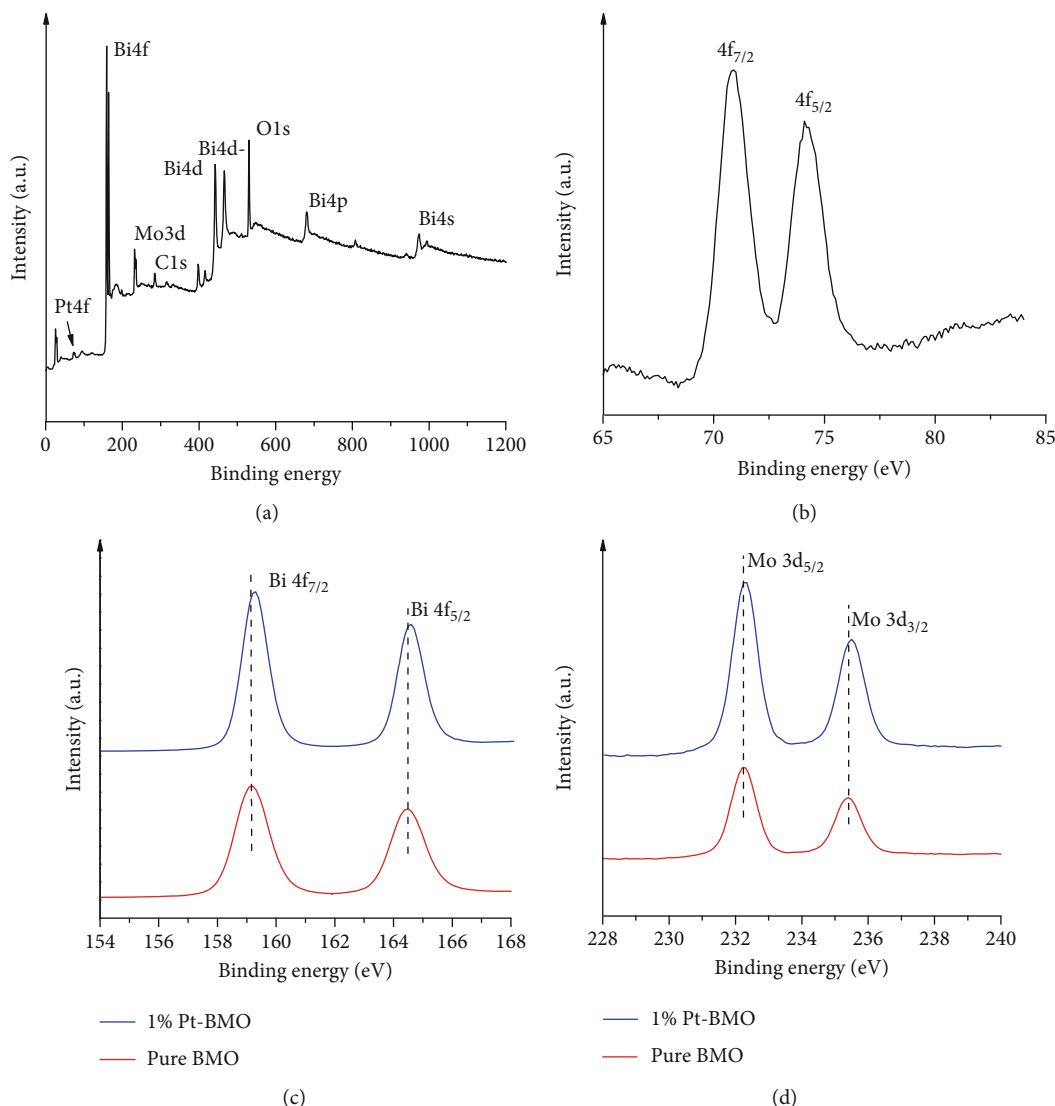


FIGURE 5: The XPS analysis. (a) The wide range spectra of 1% Pt-BMO sample; (b) high-resolution spectra of Pt4f from 1% Pt-BMO sample; high-resolution spectra of (c) Bi4f and (d) Mo3d from pure BMO and 1%Pt-BMO nanocomposites.

**3.1.5. XPS Analysis.** In order to determine the binding energy and valence of samples, the X-ray photoelectron spectroscopy was performed on 1% Pt-BMO nanocomposites, and the results were shown in Figure 5. As Figure 5(a) shows, the sample was mainly composed of three elements: Bi, Mo, and O (the signal peak of C came from atmospheric pollution). No other impurity elements appeared, which were in good agreement with the EDS analysis results. Figure 5(b) shows that the binding energies of 70.8 eV and 74.1 eV were corresponding to Pt  $4f_{7/2}$  and Pt  $4f_{5/2}$ , respectively, indicating that Pt was successfully deposited on the surface of  $\text{Bi}_2\text{MoO}_6$  with valence state of Pt(0) [39]. In Figure 5(c), the characteristic binding energy values of 159.2 eV for  $\text{Bi } 4f_{7/2}$  and 164.5 eV for  $\text{Bi } 4f_{5/2}$  illustrating that bismuth existed in the pure BMO with a trivalent oxidation state [40]. Figure 5(d) shows the binding energies of  $\text{Mo } 3d_{3/2}$  and  $\text{Mo } 3d_{5/2}$  peaks are located at 232.2 and 235.3 eV, respectively, suggesting that  $\text{Mo}^{6+}$  existed in the samples [32]. The binding energies of Bi4f and Mo3d for 1% Pt-BMO nano-

composites are  $\sim 0.1$  eV higher than those of pure BMO. These changes are probably caused by electron transferring from the surface of  $\text{Bi}_2\text{MoO}_6$  to the metal of Pt [41].

**3.1.6. Photocatalytic Performance.** The photocatalytic properties of all samples were tested by degrading RhB under visible light irradiation. As shown in Figure 6(a), the relative concentration curves of RhB are displayed. Before irradiation, an adsorption-desorption equilibrium is obtained. After visible light irradiation for 180 min, the degradation efficiency of pure BMO is about 30%. While the degradation efficiencies of 1%Pt-BMO, 2%Pt-BMO, and 5%Pt-BMO are about 50%, 70%, and 80%, respectively. Compared with pure BMO, the photocatalytic activities of Pt-BMO nanocomposites are significantly improved under visible light. In particular, 5%Pt-BMO exhibits the highest photooxidation activity. Figure 6(b) shows the stability of 5%Pt-BMO after 720 min for four consecutive cycles. 5%Pt-BMO still exhibits nearly constant RhB degradation

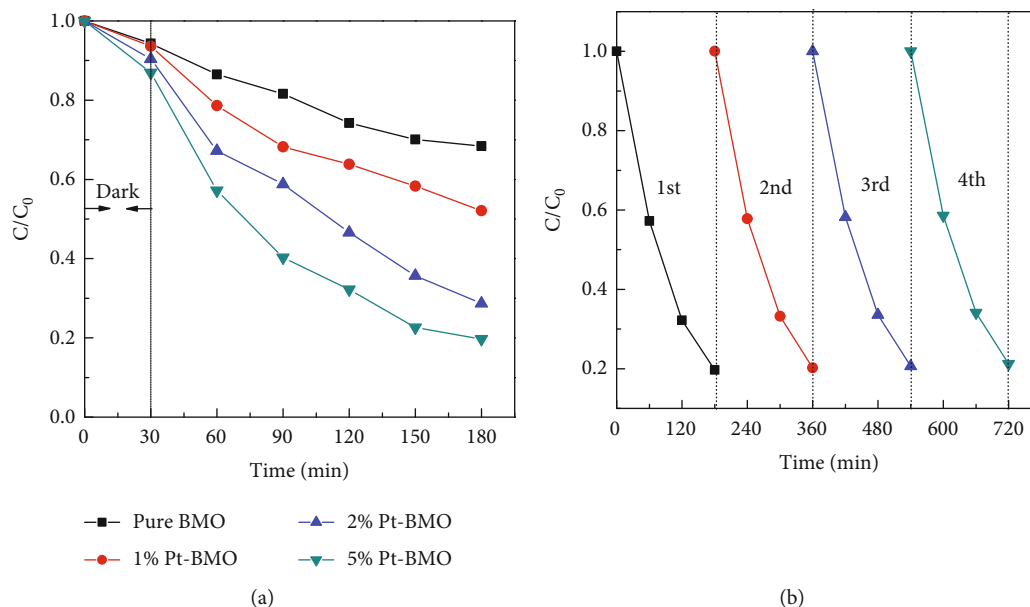


FIGURE 6: (a) Comparison of photocatalytic activities of different nanocomposites in the degradation of RhB; (b) the recyclability test of 5%Pt-BMO under visible light irradiation.

capability, indicating the high stability of 5%Pt-BMO, which is in favor of practical application.

**3.2. Biological Toxicity and PDT Efficiency for Pt-BMO Nanocomposites to HL60 Cells.** Biological toxicity results were shown in Figure 7(a). The data revealed that pure BMO, 1%Pt-BMO, 2%Pt-BMO, and 5% Pt-BMO all had certainly inhibitory effect on the cell growth. Theoretically,  $\text{Bi}_2\text{MoO}_6$  is a kind of nontoxic semiconductor. However, the size of samples was so minuscule that it had chance of penetrating cell membrane into the cytoplasm and further affected the chemical reactions between biomolecules which were important for activities of cells. For each type of nanocomposites, the relative viability of cells reduced with the increase of its concentration. For example, when concentration of pure BMO went up from  $200 \mu\text{g/mL}$  to  $1000 \mu\text{g/mL}$ , the relative viability decreased from 98.7% to 89.3%. As the values of relative viability were mostly above 90%, the pure BMO sample can be considered having good biocompatibility. When pure BMO doped with metal Pt, biological toxicity to the HL60 cells increased. At the same concentration, when the Pt content got higher, the relative viability became lower. When the 5% Pt-BMO sample with concentration of  $1000 \mu\text{g/mL}$ , the relative viability reached the lowest at 65.9%. Figure 7(b) showed the influence of irradiation on the relative viability of cells. Obviously, the relative viability fell down dramatically when the cells got irradiated. Compared with pure BMO, the Pt-BMO samples have much superior PDT efficiency, which indicating that the load of Pt on pure BMO could remarkably improve the PDT efficiency and inhibit cells liveness. Under the treatment of 5% Pt-BMO nanocomposites at  $800 \mu\text{g/mL}$ , the relative viability of cells was only 12.3%. Figure 7(c) showed the effects of different concentrations on PDT efficiency. With the increase of concentration, the efficiency of PDT gradu-

ally improved. The increasing trend slowed down when the concentration exceeded  $800 \mu\text{g/mL}$ . It was supposed that  $800 \mu\text{g/mL}$  was the limit value for the uptake of nanocomposites by HL60 cells. Under the same concentration of  $1000 \mu\text{g/mL}$ , the PDT efficiency of Pt-BMO samples was about 35%~55% higher than that of pure BMO. The order of  $P_e$  from high to low was 5%Pt-BMO > 2%Pt-BMO > 1%Pt-BMO > pure BMO. When 5% Pt-BMO sample at the concentration of  $1000 \mu\text{g/mL}$ , the PDT efficiency reached the highest at 85.2%. The reasons for high PDT efficiency at Pt-doped samples were probably that: (1) as a semiconductor with narrow band gap,  $\text{Bi}_2\text{MoO}_6$  is a superior photocatalysis naturally. (2) Due to the existence of Pt, the agglomeration for nanoparticles in water was largely reduced. So the drug intake of cells can distinctly increase, and the PDT efficiency can be improved as a result. (3) The loading of Pt on the  $\text{Bi}_2\text{MoO}_6$  surface could not only provide a plasma resonance effect for extending the light-response range to absorb more light energy but also act as electron capture to reduce the recombination of photo-induced  $e^-$  and  $h^+$  pairs, and consequently, achieving the enhanced PDT activity.

**3.3. Reactive Oxygen Species Assay.** In photodynamic therapy, after exposure to irradiation, the excited photosensitizer transferred the energy to oxygen molecules into cells, producing a large number of reactive oxygen species (ROS) with high oxidability, which destroyed the organelles and interfered with the signaling pathway, eventually leading to cells apoptosis. So, the ROS generated by irradiation has become an important indicator for evaluating photosensitizers.

The experiment analyzed the changes of ROS in different cell groups after they got irradiated. The results were shown in Figure 8. Compared with the cell group treated by pure BMO, the ROS levels in the groups treated by 1% Pt-BMO,

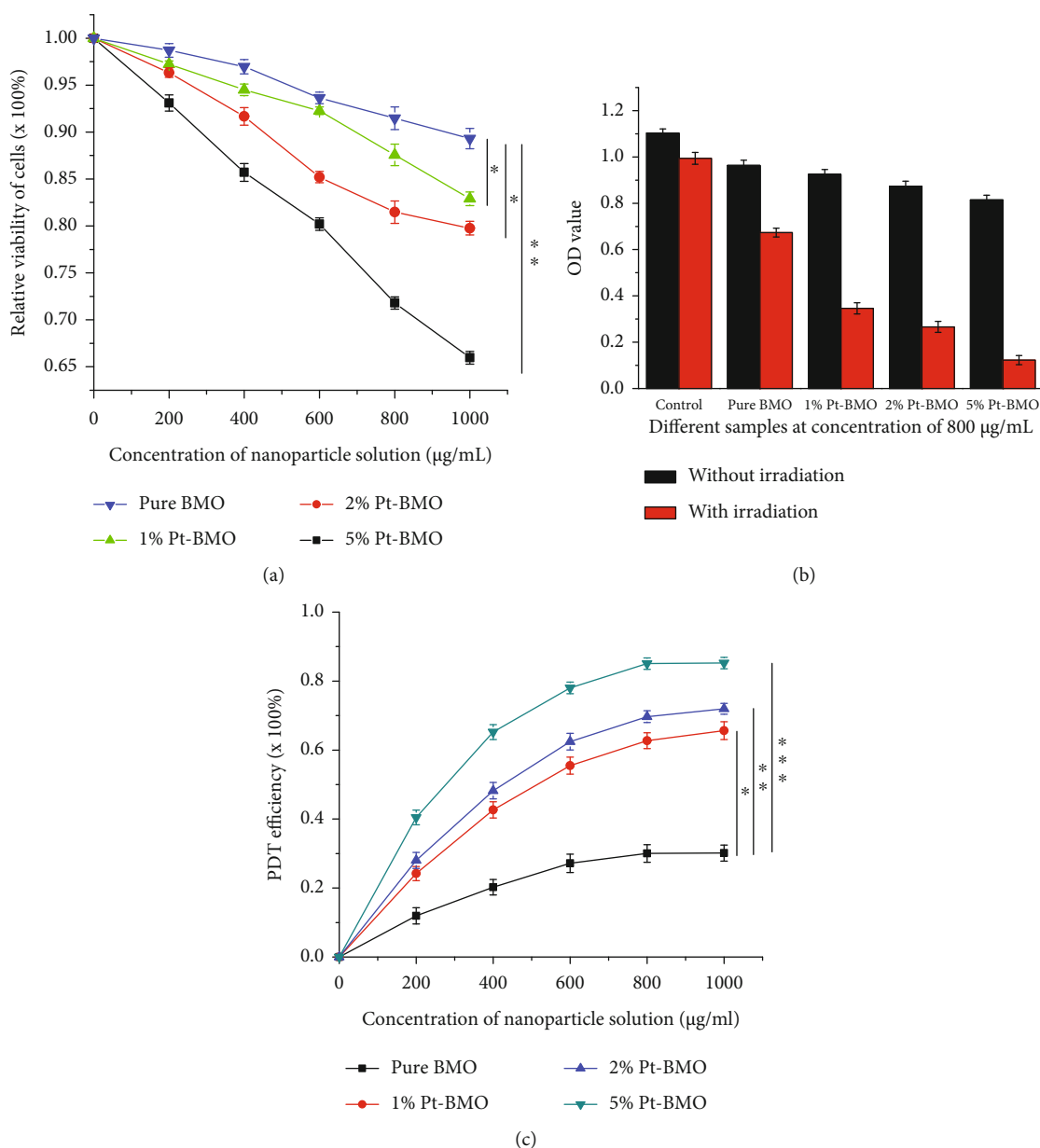


FIGURE 7: (a) The biological toxicity for Pt-BMO nanocomposites to HL60 cells; (b) the influence of different nanocomposites to HL60 cells; (c) the PDT efficiency based on different concentration. Data are presented as means  $\pm$  SD from three independent measurements. \* $P < 0.05$ , \*\* $P < 0.01$ , and \*\*\* $P < 0.001$  compared with the pure BMO treatment group.

2% Pt-BMO, and 5% Pt-BMO nanocomposites were enhanced, among which the ROS level in 5% Pt-BMO sample was the highest. Some reasons can explain this trend. First, the poor dispersion of pure BMO will lead to the limited area irradiated, so ROS will be less than samples that have superior dispersion. Second, pure BMO has a high electron-hole recombination rate, so only a small part of photoelectron can be engaged in oxidation-reduction reactions, resulting in a low content of ROS in cells. After Pt doping, the band gap width of Pt-BMO samples has been narrowed, the dispersion has been improved, and the spectral response range has been widened, which promoted the photochemical reaction to produce more ROS. This change was consistently correlated with the variation of PDT effi-

ciency, indicating that reactive oxygen species produced by nanocomposites after irradiation were the main reason for the cell apoptosis.

**3.4. Photocatalysis Mechanism of Pt-Doped  $\text{Bi}_2\text{MoO}_6$  Nanocomposites.** The principle is illustrated in Figure 9. When exposed to irradiation, the  $\text{Bi}_2\text{MoO}_6$  nanocomposites absorbed light energy, causing photoelectrons to transfer to the conduction band and holes to remain in the valence band. Some of these photogenerated electrons and holes moved to the  $\text{Bi}_2\text{MoO}_6$  surface, where the electrons reacted with oxygen to generate superoxide radical ( $\cdot\text{O}_2^-$ ), and the holes reacted with water and  $\text{OH}^-$  on the semiconductor surface to generate hydroxyl radical ( $\cdot\text{OH}$ ) with strong

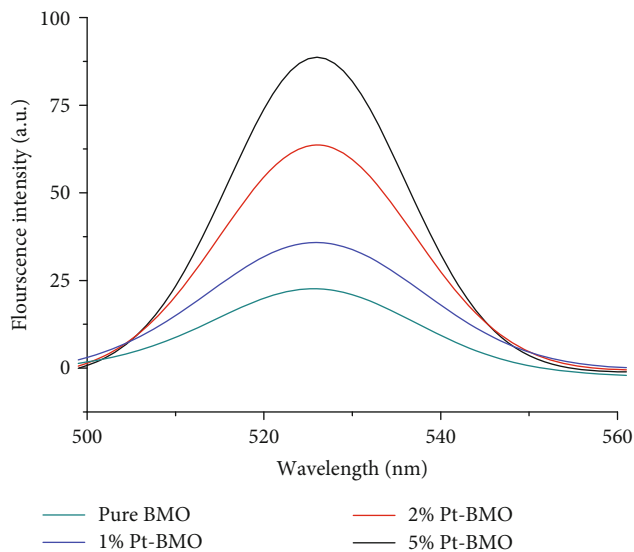


FIGURE 8: Fluorescence spectra of reactive oxygen species probe in HL60 cells after PDT for 60 min.

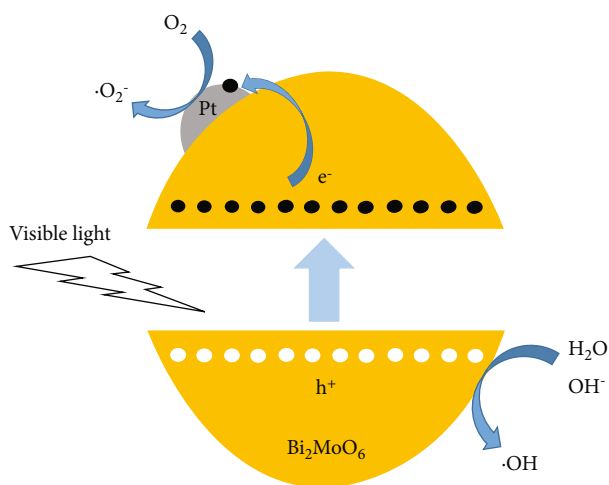
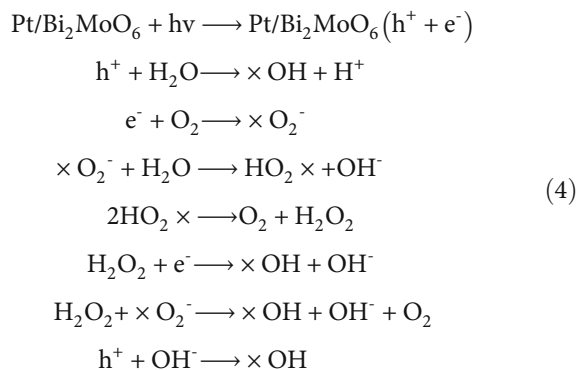


FIGURE 9: Schematic diagram of photocatalysis mechanism.

oxidizability. These free radicals and reactive oxygen species oxidized the biomolecules (such as proteins, lipids, and nucleic acids) after passing through membranes and obstructed cell's physiological and metabolic functions, eventually leading to cell apoptosis or necrosis.

When Pt was deposited on the surface of  $\text{Bi}_2\text{MoO}_6$ , the photo-generated electrons will be transferred from the surface of semiconductor material with higher fermi levels to Pt metal with lower fermi levels until the two systems achieved equilibration. At this time, the photo-generated electrons and holes were effectively separated, and the recombination rate was greatly reduced. Thus, the photocatalytic performance of Pt doped  $\text{Bi}_2\text{MoO}_6$  nanocomposites was improved, so the PDT efficiency was notably increased as a result. The inactivation process of photodynamic therapy based on Pt-doped  $\text{Bi}_2\text{MoO}_6$  nanoparticles can be explained as below:



#### 4. Conclusion

In this paper, novel Pt- $\text{Bi}_2\text{MoO}_6$  nanocomposites were prepared by solvothermal and in situ reduction method and characterized by X-ray diffraction (XRD), transmission electron microscope (TEM), X-ray photoelectron spectroscopy (XPS), and UV-Vis adsorption spectra. The results showed that synthesized nanocomposites had advantages of small size, good dispersion, and wide spectral response range. Subsequently, the biological toxicity and PDT experiments were carried out. Biological toxicity test revealed that the cell survival rate was mostly above 90% after 12 h dark treatment for pure BMO samples, indicating that it is a potential photosensitizer with good biocompatibility. With the increase of the Pt content, the toxicity of Pt-BMO samples rose slightly, but the relative viability was all above 65%. The PDT test of HL60 cells demonstrated that Pt-BMO nanocomposites had higher inactivation efficiency than pure BMO. With the raising of Pt content and the concentration of nanoparticle's solution, the PDT efficiency increased as well. When the concentration reached  $800 \mu\text{g}/\text{mL}$ , the growth trend slowed down. For 5% Pt-BMO nanocomposites at the concentration of  $1000 \mu\text{g}/\text{mL}$ , the PDT efficiency got the maximum value at 85.2%. The superior performance of Pt-BMO nanocomposites in PDT might contribute to its excellent chemical properties. High PDT efficiency and low toxicity demonstrated that the Pt-doped  $\text{Bi}_2\text{MoO}_6$  nanocomposites provided a new treatment scheme for leukemia. The problem how to improve its biocompatibility on normal cells can be solved by adding special targeted drugs. This issue might be discussed in the future work.

#### Data Availability

The data used to support the findings of this study are available from the corresponding author upon request.

#### Conflicts of Interest

The authors declare that there is no conflict of interests regarding the publication of this paper.

#### Acknowledgments

This work has been financially supported by the National Natural Science Foundation of China (Grant no.

12075090) and the Major Basic Research Project of Guangdong Province (Grant no. 2017KZDXM024).

## References

- [1] C. P. Wild, "The global cancer burden: necessity is the mother of prevention," *Nature Reviews Cancer*, vol. 19, no. 3, pp. 123–124, 2019.
- [2] F. E. Whitehead, "Letter: cancer statistics," *British Medical Journal*, vol. 1, no. 6003, pp. 223–223, 1976.
- [3] H. Kouhpeikar, A. E. Butler, F. Bamian, G. E. Barreto, M. Majeed, and A. Sahebkar, "Curcumin as a therapeutic agent in leukemia," *Journal of Cellular Physiology*, vol. 234, no. 8, pp. 12404–12414, 2019.
- [4] P. da Silva Barbosa, D. A. Duarte, M. F. Leite, and G. R. de Sant' Anna, "Photodynamic therapy in pediatric dentistry," *Case Reports in Dentistry*, vol. 2014, Article ID 217172, 5 pages, 2014.
- [5] C. W. Chu, J. H. Ryu, Y. I. Jeong et al., "Redox-responsive nanophotosensitizer composed of chlorin e6-conjugated dextran for photodynamic treatment of colon cancer cells," *Journal of Nanomaterials*, vol. 2016, Article ID 4075803, 12 pages, 2016.
- [6] Q. Q. Dou, C. P. Teng, E. Y. Ye, and X. J. Loh, "Effective near-infrared photodynamic therapy assisted by upconversion nanoparticles conjugated with photosensitizers," *International Journal of Nanomedicine*, vol. 10, pp. 419–432, 2015.
- [7] E. Y. Ye, K. Y. Win, H. R. Tan et al., "Plasmonic gold nanocrosses with multidirectional excitation and strong photothermal effect," *Journal of the American Chemical Society*, vol. 133, no. 22, pp. 8506–8509, 2011.
- [8] C. P. Teng, T. L. Zhou, E. Y. Ye et al., "Effective targeted photothermal ablation of multidrug resistant bacteria and their biofilms with NIR-absorbing gold nanocrosses," *Advanced Healthcare Materials*, vol. 5, no. 16, pp. 2122–2130, 2016.
- [9] D. P. Yang, X. Liu, C. P. Teng et al., "Unexpected formation of gold nanoflowers by a green synthesis method as agents for a safe and effective photothermal therapy," *Nanoscale*, vol. 9, no. 41, pp. 15753–15759, 2017.
- [10] S. Y. Tee, E. Y. Ye, C. P. Teng et al., "Advances in photothermal nanomaterials for biomedical, environmental and energy applications," *Nanoscale*, vol. 13, no. 34, pp. 14268–14286, 2021.
- [11] B. C. Wilson, "Photodynamic therapy for cancer: principles," *Canadian Journal of Gastroenterology*, vol. 16, no. 6, pp. 393–396, 2002.
- [12] F. U. Rehman, C. Zhao, H. Jiang, and X. Wang, "Biomedical applications of nano-titania in theranostics and photodynamic therapy," *Biomaterials Science*, vol. 4, no. 1, pp. 40–54, 2016.
- [13] D. Ziental, B. Czarczynska-Goslinska, D. T. Mlynarczyk et al., "Titanium dioxide nanoparticles: prospects and applications in medicine," *Nanomaterials*, vol. 10, no. 2, p. 387, 2020.
- [14] K. S. Al-Namshah and R. M. Mohamed, "Nd-doped Bi<sub>2</sub>O<sub>3</sub> nanocomposites: simple synthesis and improved photocatalytic activity for hydrogen production under visible light," *Applied Nanoscience*, vol. 8, no. 5, pp. 1233–1239, 2018.
- [15] Z. J. Zhang, T. T. Zheng, J. Y. Xu, H. B. Zeng, and N. Zhang, "Carbon quantum dots/Bi<sub>2</sub>MoO<sub>6</sub> composites with photocatalytic H<sub>2</sub> evolution and near infrared activity," *Journal of Photochemistry and Photobiology a-Chemistry*, vol. 346, pp. 24–31, 2017.
- [16] M. Kasinathan, S. Thiripuranthagan, A. Sivakumar et al., "Fabrication of novel Bi<sub>2</sub>MoO<sub>6</sub>/N-rGO catalyst for the efficient photocatalytic degradation of harmful dyes," *Materials Research Bulletin*, vol. 125, article 110782, 2020.
- [17] T. Ji, E. Ha, M. Z. Wu et al., "Controllable hydrothermal synthesis and photocatalytic performance of Bi<sub>2</sub>MoO<sub>6</sub> nano/microstructures," *Catalysts*, vol. 10, no. 10, p. 1161, 2020.
- [18] G. P. Zhang, D. Y. Chen, N. J. Li et al., "Fabrication of Bi<sub>2</sub>MoO<sub>6</sub>/ZnO hierarchical heterostructures with enhanced visible-light photocatalytic activity," *Applied Catalysis B-Environmental*, vol. 250, pp. 313–324, 2019.
- [19] S. L. Lin, W. Q. Cui, X. G. Li, H. Sui, and Z. S. Zhang, "Cu<sub>2</sub>O NPs/Bi<sub>2</sub>O<sub>2</sub>CO<sub>3</sub> flower-like complex photocatalysts with enhanced visible light photocatalytic degradation of organic pollutants," *Catalysis Today*, vol. 297, pp. 237–245, 2017.
- [20] T. T. Li, X. L. Hu, C. C. Liu, C. M. Tang, X. K. Wang, and S. L. Luo, "Efficient photocatalytic degradation of organic dyes and reaction mechanism with Ag<sub>2</sub>CO<sub>3</sub>/Bi<sub>2</sub>O<sub>2</sub>CO<sub>3</sub> photocatalyst under visible light irradiation," *Journal of Molecular Catalysis a-Chemical*, vol. 425, pp. 124–135, 2016.
- [21] D. Zhang, L. Chen, C. J. Xiao et al., "Facile synthesis of high {001} facets dominated BiOCl nanosheets and their selective dye-sensitized photocatalytic activity induced by visible light," *Journal of Nanomaterials*, vol. 2016, Article ID 5697672, 7 pages, 2016.
- [22] X. Y. Wang, F. C. Zhang, Y. N. Yang, Y. Zhang, L. L. Liu, and W. L. Lei, "Controllable synthesis and photocatalytic activity of nano-BiOBr photocatalyst," *Journal of Nanomaterials*, vol. 2020, Article ID 1013075, 7 pages, 2020.
- [23] D. Zhang, Y. Y. Wang, L. Chen et al., "Facile preparation and enhanced visible-light photocatalysis of ZnO arrays@BiOI nanosheets heterostructures," *Journal of Nanomaterials*, vol. 2019, Article ID 4508687, 7 pages, 2019.
- [24] F. Stelo, N. Kublik, S. Ullah, and H. Wender, "Recent advances in Bi<sub>2</sub>MoO<sub>6</sub> based Z-scheme heterojunctions for photocatalytic degradation of pollutants," *Journal of Alloys and Compounds*, vol. 829, article 154591, 2020.
- [25] F. F. Mei, J. F. Zhang, K. Dai, G. P. Zhu, and C. H. Liang, "A Z-scheme Bi<sub>2</sub>MoO<sub>6</sub>/CdSe-diethylenetriamine heterojunction for enhancing photocatalytic hydrogen production activity under visible light," *Dalton Transactions*, vol. 48, no. 3, pp. 1067–1074, 2019.
- [26] C. L. Yu, Z. Wu, R. Y. Liu et al., "Novel fluorinated Bi<sub>2</sub>MoO<sub>6</sub> nanocrystals for efficient photocatalytic removal of water organic pollutants under different light source illumination," *Applied Catalysis B-Environmental*, vol. 209, pp. 1–11, 2017.
- [27] S. Y. Wang, X. L. Yang, X. H. Zhang et al., "A plate-on-plate sandwiched Z-scheme heterojunction photocatalyst: BiOBr-Bi<sub>2</sub>MoO<sub>6</sub> with enhanced photocatalytic performance," *Applied Surface Science*, vol. 391, pp. 194–201, 2017.
- [28] M. Ratova, P. J. Kelly, G. T. West, X. H. Xia, and Y. Gao, "Deposition of visible light active photocatalytic bismuth molybdate thin films by reactive magnetron sputtering," *Materials*, vol. 9, no. 2, p. 67, 2016.
- [29] G. H. Tian, Y. J. Chen, W. Zhou et al., "Facile solvothermal synthesis of hierarchical flower-like Bi<sub>2</sub>MoO<sub>6</sub> hollow spheres as high performance visible-light driven photocatalysts," *Journal of Materials Chemistry*, vol. 21, no. 3, pp. 887–892, 2011.
- [30] D. P. Dutta, A. Ballal, S. Chopade, and A. Kumar, "A study on the effect of transition metal (Ti<sup>4+</sup>, Mn<sup>2+</sup>, Cu<sup>2+</sup> and Zn<sup>2+</sup>)-doping on visible light photocatalytic activity of Bi<sub>2</sub>MoO<sub>6</sub>

- nanorods,” *Journal of Photochemistry and Photobiology a-Chemistry*, vol. 346, pp. 105–112, 2017.
- [31] J. H. Bi, W. Fang, L. Li et al., “Ternary reduced-graphene-oxide/ $\text{Bi}_2\text{MoO}_6$ /Au nanocomposites with enhanced photocatalytic activity under visible light,” *Journal of Alloys and Compounds*, vol. 649, pp. 28–34, 2015.
- [32] R. M. Mohamed and F. M. Ibrahim, “Visible light photocatalytic reduction of nitrobenzene using Ag/ $\text{Bi}_2\text{MoO}_6$  nanocomposite,” *Journal of Industrial and Engineering Chemistry*, vol. 22, pp. 28–33, 2015.
- [33] L. N. Song, F. Ding, Y. K. Yang et al., “Synthesis of  $\text{TiO}_2/\text{Bi}_2\text{MoO}_6$  Composite for partial oxidation of aromatic alkanes under visible-light illumination,” *ACS Sustainable Chemistry & Engineering*, vol. 6, no. 12, pp. 17044–17050, 2018.
- [34] B. Zhang, J. Li, Y. Y. Gao et al., “To boost photocatalytic activity in selective oxidation of alcohols on ultrathin  $\text{Bi}_2\text{MoO}_6$  nanoplates with Pt nanoparticles as cocatalyst,” *Journal of Catalysis*, vol. 345, pp. 96–103, 2017.
- [35] H. Tominaga, M. Ishiyama, F. Ohseto et al., “A water-soluble tetrazolium salt useful for colorimetric cell viability assay,” *Analytical Communications*, vol. 36, no. 2, pp. 47–50, 1999.
- [36] K. Q. Huang, L. Chen, J. G. Deng, and J. W. Xiong, “Enhanced visible-light photocatalytic performance of nanosized anatase  $\text{TiO}_2$  doped with CdS quantum dots for cancer-cell treatment,” *Journal of Nanomaterials*, vol. 2012, Article ID 720491, 12 pages, 2012.
- [37] S. N. Gu, W. J. Li, F. Z. Wang, H. D. Li, and H. L. Zhou, “Substitution of Ce(III,IV) ions for Bi in  $\text{BiVO}_4$  and its enhanced impact on visible light-driven photocatalytic activities,” *Catalysis Science & Technology*, vol. 6, no. 6, pp. 1870–1881, 2016.
- [38] C. S. Guo, J. Xu, S. F. Wang, L. Li, Y. Zhang, and X. C. Li, “Facile synthesis and photocatalytic application of hierarchical mesoporous  $\text{Bi}_2\text{MoO}_6$  nanosheet-based microspheres,” *CrytEngComm*, vol. 14, no. 10, pp. 3602–3608, 2012.
- [39] T. H. Fleisch, G. W. Zajac, J. O. Schreiner, and G. J. Mains, “An XPS study of the UV photoreduction of transition and noble metal oxides,” *Applied Surface Science*, vol. 26, no. 4, pp. 488–497, 1986.
- [40] H. D. Li, W. J. Li, S. N. Gu, F. Z. Wang, and H. L. Zhou, “In-built  $\text{Tb}^{4+}/\text{Tb}^{3+}$  redox centers in terbium-doped bismuth molybdate nanograss for enhanced photocatalytic activity,” *Catalysis Science & Technology*, vol. 6, no. 10, pp. 3510–3519, 2016.
- [41] P. Zhang, Y. A. Yi, C. X. Yu et al., “High photocatalytic activity of lanthanum doped  $\text{Bi}_2\text{MoO}_6$  nanosheets with exposed (0 0 1) facets,” *Journal of Materials Science-Materials in Electronics*, vol. 29, no. 10, pp. 8617–8629, 2018.